

Control of bandwidth and signal-to-noise ratio for hard-x-ray self-seeded free-electron lasers


Tianyun Long^{1,2,*}, Ye Chen^{1,2}, Winfried Decking², Gianluca Geloni^{3,†}, Marc Guetg², Senlin Huang¹, Vitali Kocharyan², Shan Liu^{2,‡}, Weilun Qin², Svitozar Serkez³, and Jiawei Yan³

¹*State Key Laboratory of Nuclear Physics and Technology and Institute of Heavy Ion Physics,*

School of Physics, Peking University, Beijing 100871, China

²*Deutsches Elektronen-Synchrotron DESY, Notkestr. 85, Hamburg 22607, Germany*

³*European XFEL GmbH, Schenefeld 22869, Germany*

 (Received 6 August 2024; revised 6 February 2025; accepted 25 March 2025; published 17 April 2025)

Hard-x-ray self-seeded (HXRSS) free-electron lasers (FELs) can provide nearly fully coherent radiation pulses in the hard-x-ray domain with extremely high spectral density, which opens up new possibilities for a wide range of scientific applications such as resonant inelastic x-ray scattering, nuclear resonance scattering, and x-ray Raman spectroscopy. Spectral bandwidth and signal-to-noise ratio (SNR) are two important parameters for seeded FELs. Our theoretical and experimental studies demonstrate that the bandwidth and SNR of HXRSS FELs are closely tied to the electron beam energy profile and current profile, respectively. Nearly Fourier-transform-limited bandwidth can be realized by flattening the energy profile. For beams with asymmetric current profiles, a higher SNR can be obtained by tuning the current peak towards the head. With proper manipulation of the longitudinal phase space of the beam, decreased bandwidth and improved SNR may further enable more demanding applications requiring higher spectral resolution.

DOI: [10.1103/PhysRevApplied.23.044038](https://doi.org/10.1103/PhysRevApplied.23.044038)

I. INTRODUCTION

X-ray free-electron lasers (FELs) provide femtosecond radiation pulses with extremely high intensity and nearly full transverse coherence, making them highly valuable for applications in material science, molecular dynamics, and structural biology [1–3]. The standard operation mode for hard-x-ray FELs relies on the self-amplified spontaneous emission (SASE) mechanism, where the lasing process is initiated by electron shot noise, leading to limited longitudinal coherence.

Narrow-bandwidth x-rays with high spectral density are essential for applications such as nuclear resonance scattering, x-ray Raman spectroscopy, and coherent control

experiments [4–7]. Externally seeded FELs are proposed to generate coherent pulses with significantly increased spectral density, where external lasers are employed to trigger the FEL frequency up-conversion [8,9]. However, these techniques are currently not applicable in the hard-x-ray region below the nanometer range. Self-seeding schemes can expand the photon energy to the hard-x-ray regime [10–14]. In a typical hard-x-ray self-seeded (HXRSS) FEL system, the undulator is split into two parts. The first part is used to generate SASE, which is then filtered by a monochromator by Bragg reflection or forward Bragg diffraction [15,16] to obtain a coherent seeding wake. The electron beam is delayed by the bypass chicane to overlap with the seeding wake at the entrance of the final undulator section to enable seeding amplification to produce nearly fully coherent radiation pulses. Adopting a compact monochromator section utilizing a crystal with Bragg forward diffraction is an efficient method for HXRSS FEL, where the filtered SASE has a long trailing monochromatic wake that can be used as a seed with a small delay for the electron beam [10]. Compared with current synchrotron facilities, the unique combination of HXRSS FEL and high-repetition-rate operation enables the average brightness of the radiation to be more than 2

*Contact author: longtianyun@pku.edu.cn, tianyun.long@desy.de

†Contact author: gianluca.aldo.geloni@xfel.eu

‡Contact author: shan.liu@desy.de

Published by the American Physical Society under the terms of the [Creative Commons Attribution 4.0 International](https://creativecommons.org/licenses/by/4.0/) license. Further distribution of this work must maintain attribution to the author(s) and the published article's title, journal citation, and DOI.

orders of magnitude higher [14,17,18], opening up new possibilities for photon-hungry experiments like resonant x-ray excitation [19].

Further enhancing the spectral resolution of HXRSS FELs is crucial for applications such as Mössbauer spectroscopy [20,21] and inelastic x-ray scattering [22,23]. Achieving higher spectral density and purity necessitates low spectral bandwidth and a high signal-to-noise ratio (SNR) from HXRSS FELs. Here, SNR is defined as the ratio between the pulse energy of the seeding signal [centered at the target photon energy and with a total bandwidth of around 2 times the seeding full width at half maximum (FWHM) bandwidth] and the noise (total pulse energy minus the seeding signal energy). Achieving low spectral bandwidth and higher SNR still faces challenges and is under active study [13,24]. Although the HXRSS FEL utilizes a coherent seed actively filtered by a monochromator with a narrow bandwidth, the amplified FEL is experimentally observed with a larger bandwidth than the seed bandwidth, which hinders further improvements in realizing a Fourier-transform-limited bandwidth with a longer lasing part (a longer beam lasing window) in the final amplification stage. For higher purity realization, although the laser heater is optimized to mitigate microbunching instabilities to get rid of the spectral pedestal [13,25–27], the chosen seeding wake may also contain SASE components that degrade the purity of the amplified seed. The monotrailing wake is generated from the convolution between the impinging SASE pulse and the crystal impulse response, and it has high spectral purity with a large delay from the main SASE pulse at the expense of a quickly reducing intensity. For a small delay with a relatively high intensity, the spectrum contains SASE components that can finally contribute as noise.

In this paper, we explore the impact of longitudinal phase space (LPS) on spectral bandwidth and SNR for HXRSS FELs. It is found that the electron beam energy profile has an important impact on the central wavelength and bandwidth of the amplified HXRSS FEL due to the undulator longitudinal dispersion. Spectral SNR is mainly affected by the trade-off between seeding wake purity, where a large delay is preferred, and the seeding wake strength, where a small delay is desired. Electron beams with peak currents towards the head for beams with asymmetric current profiles are found to be beneficial for higher SNR. With proper beam LPS manipulation, the decreased bandwidth and improved SNR can bring an increase in spectral brightness and purity.

This paper is organized as follows. In Sec. II we present a general theoretical analysis for the HXRSS FEL bandwidth and SNR study with FEL simulations carried out with ideal electron beams. In Sec. III we present start-to-end simulations for the European XFEL. We show experimental results in Sec. IV and summarize in Sec. V.

II. THEORETICAL ANALYSIS AND SIMULATION WITH IDEAL CASES

In this section, we study the spectral bandwidth and the SNR of HXRSS FEL pulses from ideal electron beams. FEL simulations in this paper are carried out with GENESIS 1.3 [28]. Spectral bandwidth is closely related to the electron energy profile: linear energy chirps will mainly cause the central wavelength to shift, while nonlinear chirps will broaden the bandwidth. A flat electron beam energy profile is desired for the realization of a nearly Fourier-transform-limited bandwidth in HXRSS FELs. SNR is found to be related to the beam current profile with an optimized delay, and when the peak current is located at the head, the SNR tends to be larger for HXRSS FELs.

A. Electron beam energy profile impact on HXRSS FEL bandwidth

The free-electron lasing process can be initiated in different ways, such as, by electron shot noise (SASE), an incident seeding light wave, a periodic charge density modulation, or energy modulation of the electron beam. During continuous interaction with the electron beam along the undulator, radiation is amplified in the high-gain lasing process, where the resonant central wavelength λ_r is

$$\lambda_r = \frac{\lambda_u}{2\gamma^2} \left(1 + \frac{K^2}{2} \right), \quad (1)$$

with λ_u the undulator period, K the undulator parameter, and γ the electron Lorentz factor. For an FEL operated in SASE mode, the relative spectral bandwidth near saturation is on the order of $\Delta\lambda/\lambda_r \sim \rho$, with ρ the FEL parameter (Pierce parameter), which is typically on the order of 10^{-3} for the hard-x-ray case. For seeded FELs, the bandwidth can be decreased by at least one order of magnitude due to the improved longitudinal coherence of the seed signal, resulting in high spectral density radiation. The energy detuning tolerance for seeded FELs is estimated to be $\Delta\gamma/\gamma \sim \rho/2$. The longitudinal dispersion of the undulator is

$$R_{56,\text{undu}}(z) = -\frac{z}{\gamma^2} \left(1 + \frac{K^2}{2} \right), \quad (2)$$

with z the propagation distance in the undulator. At the beginning of the final seeding amplification stage, the electron beam develops microbunching with a period that is the same as the seed wavelength λ_r . However, if there is a correlated electron beam energy chirp, the bunching distance can be modulated during the lasing process due to the undulator longitudinal dispersion. Given a linear chirp of $\alpha = d\delta/ds$, where $\delta = (\gamma - \gamma_0)/\gamma_0$ is the electron fractional energy offset, γ_0 is the reference Lorentz factor, and s the longitudinal coordinate along the electron beam (the

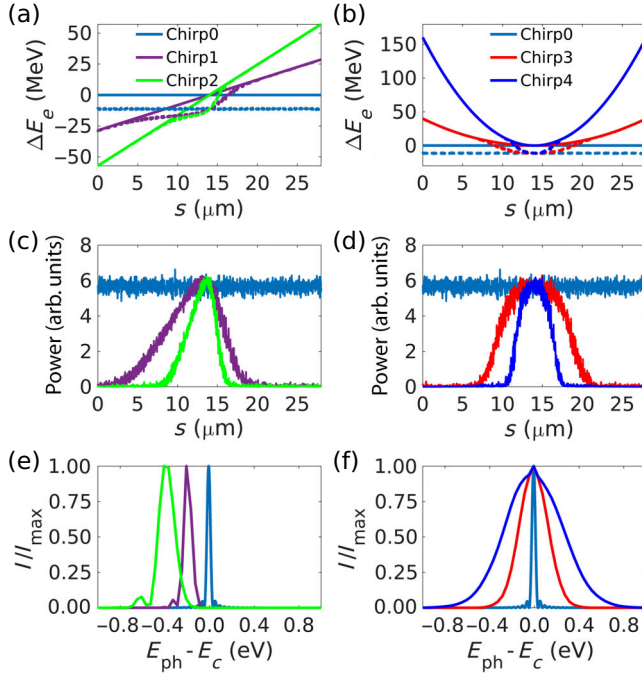


FIG. 1. Simulation results for ideal beams with different energy profiles. Beam head is assumed to be towards the right in this paper. (a),(b) Initial (solid curves) and final (dashed curves) beam slice energy distribution. (c),(d) Radiation power profile. (e),(f) The corresponding normalized spectra.

beam head is assumed to have a larger positive s value than the beam tail in this paper), the modulated bunching distance can be expressed as

$$\lambda_M = \lambda_r(1 - \alpha R_{56, \text{undu}}), \quad (3)$$

which is also the modified radiation wavelength. The modulation in Eq. (3) corresponds to a frequency shift, which will increase (with $\alpha < 0$) or decrease (with $\alpha > 0$) the original target photon energy E_{ph} by an amount around $\Delta E_{\text{ph}} = \alpha R_{56, \text{undu}} E_{\text{ph}}$. When the correlated electron beam energy chirp is nonlinear, different lasing parts will cause different photon energy shifts, which can finally result in a broadening of the seeded FEL spectrum.

Figures 1 and 2 show the FEL simulation results for seeded FEL with a target central photon energy of $E_c = 9$ keV using an ideal beam and ideal seeding radiation with a flat power profile for different electron energy profile configurations. All ideal beams have a central beam energy of $E_e = 16.3$ GeV, and a 5-kA flat-top current profile with a length of $28 \mu\text{m}$. The spectra are shown at the position near saturation without undulator tapering.

For different linear chirps of 0, 2, and 4 MeV/ μm , namely, $\delta = \alpha_i(s - s_0)$ with $s_0 = 14 \mu\text{m}$, $\alpha_0 = 0 \text{ m}^{-1}$, $\alpha_1 = 125.4 \text{ m}^{-1}$, $\alpha_2 = 250.8 \text{ m}^{-1}$ (indicated by Chirp0, Chirp1, Chirp2, respectively), the lasing windows and the

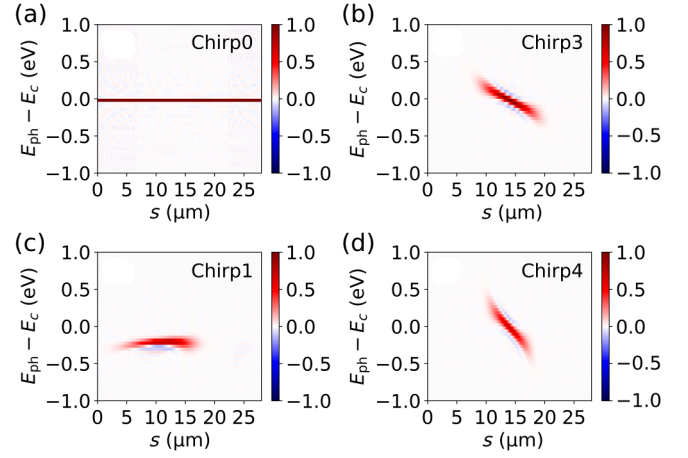


FIG. 2. Wigner distributions for seeded free-electron lasers with different electron beam energy profiles.

spectra are different. With a larger linear chirp, the lasing window is shorter due to the constraint on energy detuning. The lasing window is directly shown by the radiation power profile in Fig. 1(c) and indicated by the beam slice energy loss shown by the dashed curves in Fig. 1(a). When there is no energy chirp, the seeded FEL spectrum has the same central photon energy as the seed. However, with a linear energy chirp, the central photon energy of the amplified seeded spectrum shifts. A positive chirp will cause the microbunching period to stretch, resulting in a lower photon energy. The spectral shifts at $z = 55 \text{ m}$ for Chirp1 and Chirp2 are about -0.21 and -0.41 eV from the simulation. The undulator dispersion is estimated to be $R_{56, \text{undu}} = 0.32 \mu\text{m}$ from Eq. (2) and we get $\Delta E_{\text{ph}} = -0.37$ and -0.74 eV for these two chirp values according to Eq. (3). During the photon energy modulation, the generated radiation will lag the shift process; therefore, the obtained central photon energy deviation from simulation is less than that obtained from Eq. (3). This phenomenon is similar to that found in a soft-x-ray seeded FEL study that found the effective undulator dispersion to be only two-thirds of $R_{56, \text{undu}}$ [26]. Here, the effective undulator dispersion is about one-half of $R_{56, \text{undu}}$. The shifted seeding spectra also have a broadened bandwidth, as shown in Fig. 1(e). The spectrum FWHM bandwidth increases from 0.04 eV for Chirp0 to 0.08 eV for Chirp1 and to 0.17 eV for Chirp2. This is mainly caused by the lasing window being shrunk due to detuning effects. Additionally, the beam energy loss during the lasing can modify the correlated energy chirp, as shown by the dashed curves in Fig. 1(a), which may slow down or speed up the shift for different lasing parts, explaining the small spikes in Fig. 1(e). The modified correlated energy chirp also results in an asymmetry for the power profile with a longer lasing window in the tail in Fig. 1(c).

For an energy profile with a nonlinear chirp, parabolic shapes with $\delta = \alpha_i(s - s_0)^2$, $\alpha_3 = 1.25 \times 10^7 \text{ m}^{-2}$, $\alpha_4 = 5.02 \times 10^7 \text{ m}^{-2}$ (indicated by Chirp3 and Chirp4), are considered in the simulations, as shown in Figs. 1(b), 1(d), and 1(f). Since these parabolic energy profiles have symmetric lasing parts with continuously changing chirp values within the lasing window, the resulting power profiles and spectra are symmetric. The spectral bandwidth increases from 0.04 eV for Chirp0 to 0.3 eV for Chirp3 and to 0.6 eV for Chirp4.

In contrast with Chirp1 and Chirp2, the bandwidth increases for Chirp3 and Chirp4 are quite large and this is caused mainly by the frequency chirp within the radiation pulse, where the shortening of the radiation pulse due to the shrunk lasing window plays only a minor role. Detailed seeded FEL radiation analysis is shown in Fig. 2 from the Wigner distribution [29,30]

$$W(t, \omega) = \int_{-\infty}^{\infty} E(t + \tau/2) E^*(t - \tau/2) e^{-i\omega\tau} d\tau, \quad (4)$$

which is widely used in the FEL community for time-frequency analysis of electric field $E(t)$ [31–34]. We can see clearly from this time-frequency analysis how the photon energy is modulated along the beam slices. The corresponding power profile and spectra (shown in Fig. 1) are projections of the Wigner distribution on the time axis and frequency axis, respectively. For the case with no chirp [Fig. 2(a)], the radiation has a stable amplified signal with the same wavelength as the seed over the whole of the beam's longitudinal axis; when projected onto the frequency axis, the spectrum shows a narrow bandwidth and no shift for E_{ph} . For case with a linear chirp α_1 [Fig. 2(c)], the Wigner distribution shifts along the frequency axis towards lower E_{ph} values with a shrunk lasing window. For an electron beam with a parabolic energy profile, the Wigner distribution [Figs. 2(b) and 2(d)] presents a linear tilt, since the photon energy shift (ΔE_{ph}) is proportional to the chirp value, which changes linearly along the beam's longitudinal axis. When projected onto the frequency axis, the spectral bandwidth is broadened considerably.

The linear electron beam energy chirp will mainly cause a frequency shift for the seeded FEL and the nonlinear energy profile will usually induce a spectral bandwidth increase, both of which can introduce a reduction in the lasing window, causing less efficient FEL performance with lower pulse energy. Electron beam energy chirps should be avoided for the realization of seeded FELs with stable central photon energy and high spectral density. Multiple spectral spikes may appear if the nonlinear energy profile has an abrupt chirp change rather than a smooth change for different beam parts. An extreme example is a V-shaped energy profile, which may cause the spectrum to split into two spikes. Spike number analysis can therefore serve as an indication of the energy profile smoothness and

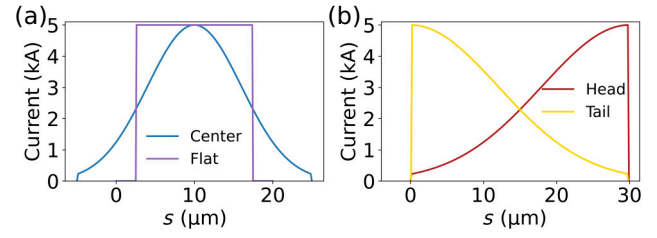


FIG. 3. Different current profiles used for ideal beam simulations.

we will adopt this method for spectral data analysis later. Fine-tuning the electron LPS for the main lasing part is important for seeded FELs and a flat energy profile is a prerequisite for a Fourier-limited seeded FEL realization.

B. Electron beam current profile impact on HXRSS FEL SNR

Another important parameter for seeded FELs is the SNR value. The seed signal in many HXRSS FELs is generated by filtering SASE radiation through a diamond crystal in transmission geometry. This leads to a seeding wake following the main SASE pulse with a decreasing intensity. The delay is fine-tuned to get a good overlap between the seeding wake and the electron bunch in the final amplification stage. If the delay is too small, there is a high chance that a non-negligible part of the beam will overlap with the leading SASE. If the delay is too large, the seeding wake may be too weak to lead to efficient amplification. One cannot increase the impinging SASE pulse energy too much to get a higher seeding wake, since this may spoil the beam during the SASE stage and even cause a heat load issue in the crystal. Therefore, there is a trade-off between seeding strength and seeding purity. A cascaded HXRSS FEL configuration is one solution to improve the SNR while controlling the heat load [17,18]. Here we study the control of the SNR for HXRSS FELs via beam current profile manipulation, and we find a higher SNR is obtained when the peak current is located towards the head for asymmetric current profiles.

We consider different current profiles, as shown in Fig. 3: a Gaussian profile, a flat-top profile, and half-Gaussian profiles with the current peak located at the head and tail (indicated by Center, Flat, Head, and Tail, respectively). All current profiles have a peak current of 5 kA, bunch charge of 250 pC, and an ideal flat electron beam energy profile with central beam energy of $E_e = 16.3 \text{ GeV}$. The SASE pulse generated in the first stage has a pulse energy around 30–40 μJ for all cases. A 100-μm-thick diamond crystal with (110) cut and (004) reflection plane is used for monochromatization at a target photon energy of 9 keV. The delay is optimized separately to achieve the highest peak spectral intensity at a location near the saturation position in the final seeding amplification stage.

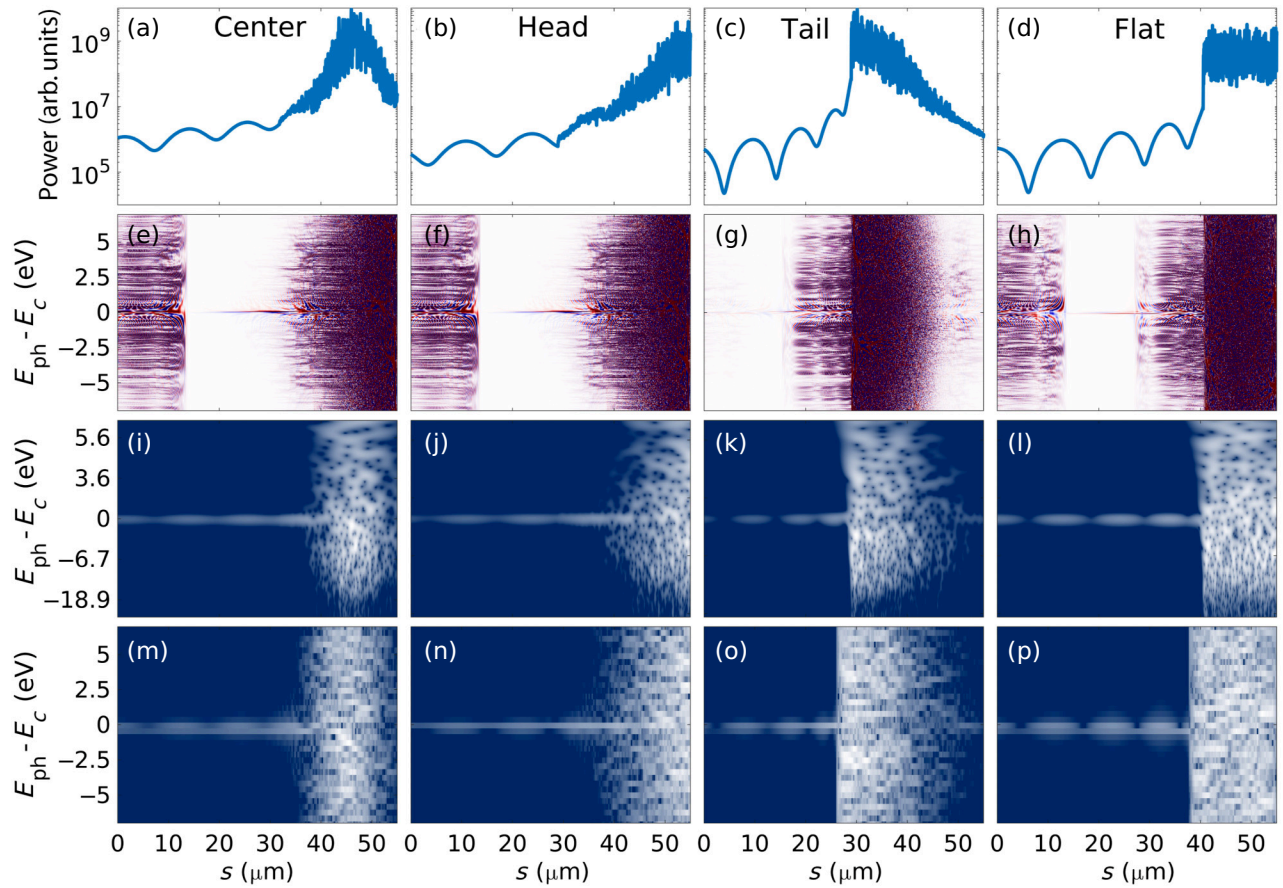


FIG. 4. Time-frequency analysis for a self-amplified spontaneous emission pulse with trailing wake just after the monochromator for cases with different current profiles. (a)–(d) Power profile. (e)–(h) Wigner distribution with similar colormap as in Fig. 2. (i)–(l) Continuous wavelet transform. (m)–(p) Short-time Fourier transform. The brighter regions show higher values in (i)–(p).

Time-frequency analyses are carried out to find the optimal delay considering the trade-off between seeding signal strength and purity. We empirically find that the Wigner distribution is suitable for pulses with a relatively homogeneous power distribution. However, for pulses with a drastically changing power profile, like the filtered SASE pulse trailed by a long weak wake, the time-frequency description from the Wigner distribution can suffer from the interference [35] between the weak wake and strong leading SASE pulse. In addition to the Wigner distribution, we carry out two other time-frequency analyses, continuous wavelet transform [35–37] and short-time Fourier transform, for the filtered pulses with different current profiles, as shown in Fig. 4. Here, the continuous wavelet transform is obtained using the analytic Morse wavelet with the symmetry parameter of 9, the time-bandwidth product value of 360, and 40 voices per octave. The short-time Fourier transform is obtained using a square window with a window length of 3 μm . The time-frequency contents are visually blurred near both ends of the wake for the Wigner distribution, as shown by Figs. 4(e)–4(h), while continuous wavelet transform [Figs. 4(i)–4(l)] and

short-time Fourier transform [Figs. 4(m)–4(p)] are unaffected and can present where the seeding dominates over the SASE background.

For these ideal beams (Center, Head, Tail, and Flat cases), the SASE generated from the first stage inherits the current profile, and the seeding wake comes from convolution between the SASE pulse and crystal impulse response. When the peak current is at the head and the seeding signal from the strong SASE at the head dominates over the weak SASE close to the tail, the beam slice will have a seed-like spectrum, as shown by Figs. 4(b), 4(j), and 4(n). Therefore, in this case, the delay does not need to be as large as the SASE pulse length (30 μm here) to guarantee both satisfactory seeding wake strength and purity. When the peak current is at the tail, the SASE is strong at the tail and the seeding wake from the front SASE slices is weaker, hence a clean seeding signal is only observed totally out of the SASE pulse range, as shown by Figs. 4(c), 4(k), and 4(o). In this case, if one wants the whole electron beam to overlap with the seeding wake with high purity, the delay should be at least as large as the SASE pulse length (30 μm here). When the delay is smaller than

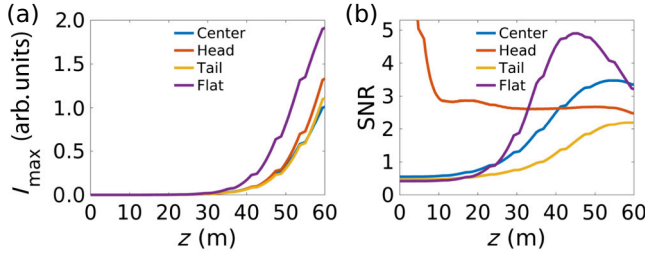


FIG. 5. Hard-x-ray self-seeded free-electron laser performance at the final seeding amplification stage before saturation for ideal beams with different current profiles. Data sets are averaged over 50 simulation runs. (a) Peak spectral density evolution along the undulator. (b) Signal-to-noise ratio (SNR) evolution along the undulator.

the SASE pulse length, there will be overlap between the strong SASE part and the low current beam part, presenting a severe trade-off between the seeding wake strength and purity. When the beam has a Gaussian profile, the seeding signal will dominate over the SASE at the SASE tail [Center case, Figs. 4(a), 4(i), and 4(m)], similar to the case of the Head, but with a position further down towards the tail. When the current profile has an ideal flat top, the seeding signal purity is similar to the case with the peak current at the tail, but here the SASE pulse is much shorter (15 μm here), as shown by Figs. 4(d), 4(l), and 4(p), and with this relatively small delay, both strength and purity requirements can be met for the seeding wake.

The delay is optimized to achieve the highest spectral density in FEL simulations for individual cases with different current profiles: 17.5 μm for Center, 20 μm for Head, 25 μm for Tail, and 15 μm for Flat. The seeding amplification process before saturation is shown in Fig. 5. It can be seen that Flat case has the highest peak spectral density and the highest SNR. The Tail and Center cases have the lowest peak spectral density, while the Center case has a higher SNR in the later stage than the Head case. For asymmetric current profiles, the Head case dominates over the Tail case for both peak spectral density and SNR.

III. START-TO-END SIMULATION

In reality, it is challenging or even impossible to obtain a perfectly symmetric flat current profile with a flattened energy profile. Collective effects, such as space-charge

effects, coherent synchrotron radiation, and wakefield effects will have a large impact on the beam quality during beam acceleration and compression along the transport system. Here we show start-to-end simulation studies for HXRSS FELs at the European XFEL. The European XFEL is an x-ray FEL facility based on a superconducting linear accelerator [38,39]. A HXRSS system is installed in the SASE2 beamline with the possibility of a cascaded HXRSS FEL setting to mitigate heat load issues for low photon energy and high-repetition-rate operation [14,17,18,40,41]. A schematic layout for the European XFEL with the SASE2 beamline is shown in Fig. 6. The gun is followed by the energy booster (A1), linearizer (AH1), laser heater (LH), dogleg (DL), three bunch compressors (BC0, BC1, BC2) with three interleaved acceleration sections (L1, L2, L3), the collimation section (CL), and the beam switchyard arc to transport selected electron bunches to the SASE2 beamline, where a cascaded HXRSS FEL system is installed. There is also a passive streaker system for the longitudinal phase space measurement downstream of SASE2 [42].

Here we follow the start-to-end simulation studies from Refs. [43–46]. We denote the electron energy offset at the gun exit as $\delta_0 = (E - E_0)/E_0 = \delta'_0 s + \delta''_0 s^2/2 + \delta'''_0 s^3/6$, with particle energy E , reference particle position $s = 0$, and reference energy E_0 . With a nominal setting for the bunch compressors, we tune the voltage (V_{A1} , V_{AH1} , V_{L1} , V_{L2}) and phase (ϕ_{A1} , ϕ_{AH1} , ϕ_{L1} , ϕ_{L2}) of A1, AH1, L1, and L2 to control the electron beam LPS evolution. There are other parameter sets describing the acceleration and compression process that are equivalent to these eight rf parameters. The first parameter set is $(E_1, E_2, E_3, Z_1, Z_2, Z_3, Z'_3, Z''_3)$ [43,46], where (E_1, E_2, E_3) are the reference electron energies at bunch compressor entrances, (Z_1, Z_2, Z_3) are global inverse compressions ($Z_i = \partial s_i / \partial s$ with s_i the particle longitudinal position within the beam at the i th compressor exit, s the initial position at the gun exit), $Z'_3 = \partial Z_3 / \partial s$ and $Z''_3 = \partial^2 Z_3 / \partial s^2$ are first- and second-order derivatives of the inverse global compression Z_3 . Another equivalent set is $(E_1, E_2, E_3, \alpha_1, \alpha_2, \alpha_3, Z_2, Z_3)$ [44,45], where $(\alpha_1, \alpha_2, \alpha_3)$ are the first (chirp), second (curvature), and third (skewness) derivatives of the fractional energy offset at the exit of AH1, namely, $\delta_{AH1} = (E - E_1)/E_1 = \alpha_1 s + \alpha_2 s^2/2 + \alpha_3 s^3/6$. $(E_1, \alpha_1, \alpha_2, \alpha_3)$ are equivalent to $(V_{A1}, \phi_{A1}, V_{AH1}, \phi_{AH1})$. The last acceleration section L3 is tuned to a crest and the final electron energy is set to 16.5 GeV here.

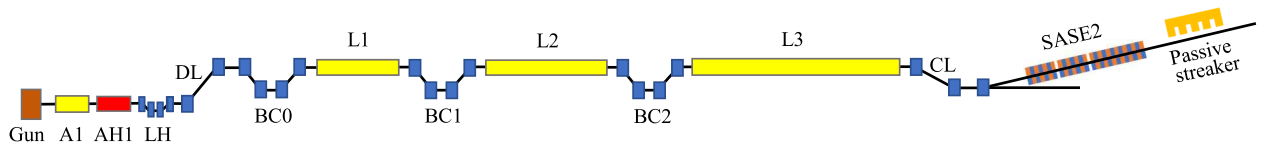


FIG. 6. Schematic layout for the European XFEL with SASE2 beamline.

We use all three sets of parameters here for the LPS manipulation study. It has been shown [43–46] that the final electron beam energy profile can be controlled effectively by tuning $(\alpha_1, \alpha_2, \alpha_3)$ to modify the local linear and nonlinear chirps, and the current profile is closely related to (Z_3, Z'_3, Z''_3) , where Z_3 is related to the peak current value, and Z'_3 and Z''_3 correspond to the current profile symmetry. Theoretically, by optimizing α_2 and α_3 we may flatten the energy profile, by tuning Z'_3 to a positive value we may get the peak current located at the tail, and by tuning Z'_3 to a negative value we may get the peak current located at the head. However, due to the collective effects, the energy profile and current profile are closely correlated with each other and it is quite challenging to optimize them separately. We empirically find it is relatively easier to use these two different parameter sets for energy profile tuning and current profile tuning, respectively.

Start-to-end simulations are carried out with the multiphysics software package OCELOT [47] in an iterative way, and the optimized parameters are listed in Table I for four cases (Case1–Case4) with different LPS distributions. LPS and corresponding HXRSS FEL simulations each averaged over 50 runs (with optimized delay and undulator tapering) are shown in Fig. 7. Case1 and Case2 are chosen to present the impact of different energy profiles on the HXRSS bandwidth, while Case3 and Case4 are chosen to present the impact of different current profiles on the HXRSS SNR. Key parameters from the HXRSS FEL simulations are listed in Table II. It is worth mentioning that, in all these cases, the peak current is kept at around the nominal value of 5 kA, which constrains the variation range of different parameters.

For Case1 and Case2, as shown in the first two columns in Fig. 7, we tune the curvature (330 m^{-2} for Case1 and 300 m^{-2} for Case2) and fine-tune the cubic coefficients to get different energy chirps within the main lasing window. For Case1, the energy profile has a chirp with a value range of -6.7 to $6.3 \text{ MeV}/\mu\text{m}$ within the lasing window and the spectral bandwidth is 0.32 eV at $z = 58 \text{ m}$ and 0.36 eV at $z = 114 \text{ m}$. For Case2, the energy profile is optimized to have a smaller chirp with a value range of -3.9 to $5.9 \text{ MeV}/\mu\text{m}$ and the spectral bandwidth is 0.24 eV at $z = 58 \text{ m}$ and 0.28 eV at $z = 114 \text{ m}$, as shown in Figs. 7(m) and 7(n). The spectral bandwidth in Case2 is smaller than in Case1 due to a smaller chirp, which qualitatively agrees with the theoretical analysis from Sec. II A.

By tuning the inverse global compression parameters (Z_3, Z'_3, Z''_3) we get different distributions with the peak current at the tail (Case3, $Z'_3 = 1.92 \text{ m}^{-1}$) and at the head (Case4, $Z'_3 = -2.93 \text{ m}^{-1}$), as shown in the last two columns in Fig. 7. We can see that having the peak current at the head is better than at the tail for both SNR and peak spectral density I_{max} : for Case3, the SNR is 2.22 and $I_{\text{max}} = 0.41 \text{ mJ/eV}$ at $z = 58 \text{ m}$ and the SNR is 1.42 and

TABLE I. Start-to-end simulation parameters.

Parameter	Case1	Case2	Case3	Case4	Unit
Electron beam					
Charge		250			pC
E_0		6.65			MeV
δ'_0		2.04			m^{-1}
δ''_0		-815			m^{-2}
δ'''_0		-150453			m^{-3}
E_1		130			MeV
α_1	-7.91	-7.91	-7.91	-7.91	m^{-1}
α_2	330	300	420	270	m^{-2}
α_3	200108	150107	175105	175104	m^{-3}
E_2		700			MeV
E_3		2400			MeV
Z_1	0.3385	0.3354	0.3367	0.3370	
Z_2	0.0482	0.0478	0.0480	0.0480	
Z_3	0.0019	0.0025	0.0028	0.0028	
Z'_3	-0.86	-1.91	1.92	-2.93	m^{-1}
Z''_3	4946	3666	3037	5025	m^{-2}
E_4		16500			MeV
Bunch compressor					
$R_{56, \text{LH}+\text{DL}+\text{BC0}}$		-85.78			mm
$R_{56, \text{BC1}}$		-50.04			mm
$R_{56, \text{BC2}}$		-29.91			mm
rf					
V_{A1}	203.08	176.91	191.11	188.60	MV
ϕ_{A1}	-44.23	-34.87	-39.41	-40.06	deg
V_{AH1}	63.74	51.28	58.38	57.08	MV
ϕ_{AH1}	110.30	151.10	114.56	111.54	deg
V_{L1}	658.22	658.15	658.28	658.14	MV
ϕ_{L1}	29.98	29.97	29.99	29.96	deg
V_{L2}	1703.91	1706.78	1704.10	1708.72	MV
ϕ_{L2}	-1.90	-3.35	-2.75	-4.38	deg

$I_{\text{max}} = 1.20 \text{ mJ/eV}$ at $z = 114 \text{ m}$; for Case4, the SNR is 3.46 and $I_{\text{max}} = 1.39 \text{ mJ/eV}$ at $z = 58 \text{ m}$ and the SNR is 2.09 and $I_{\text{max}} = 4.58 \text{ mJ/eV}$ at $z = 114 \text{ m}$. Here we note that when the peak current is at the tail, an extra large chirp (with a chirp value range of -10.8 to $6.2 \text{ MeV}/\mu\text{m}$) is introduced during the transport in the beam switchyard arc due to the collective effects [48–51], resulting in a larger spectral bandwidth. Beam transport through the arc introduces additional transverse kicks, which are particularly pronounced in Case3. This results in a reduced lasing window and, consequently, lower pulse energy, as illustrated in Figs. 7(g) and 7(o).

We list detailed parameters for these four cases in Tables I and II for comparison. These parameters also confirm the complexity of the close relationship between the electron beam energy profile and current profile, which together have a complicated impact on the HXRSS FEL performance. In Sec. II, we use ideal beam distributions to show how the energy and current profiles separately affect spectral bandwidth and SNR. However, start-to-end simulations show how these factors are correlated,

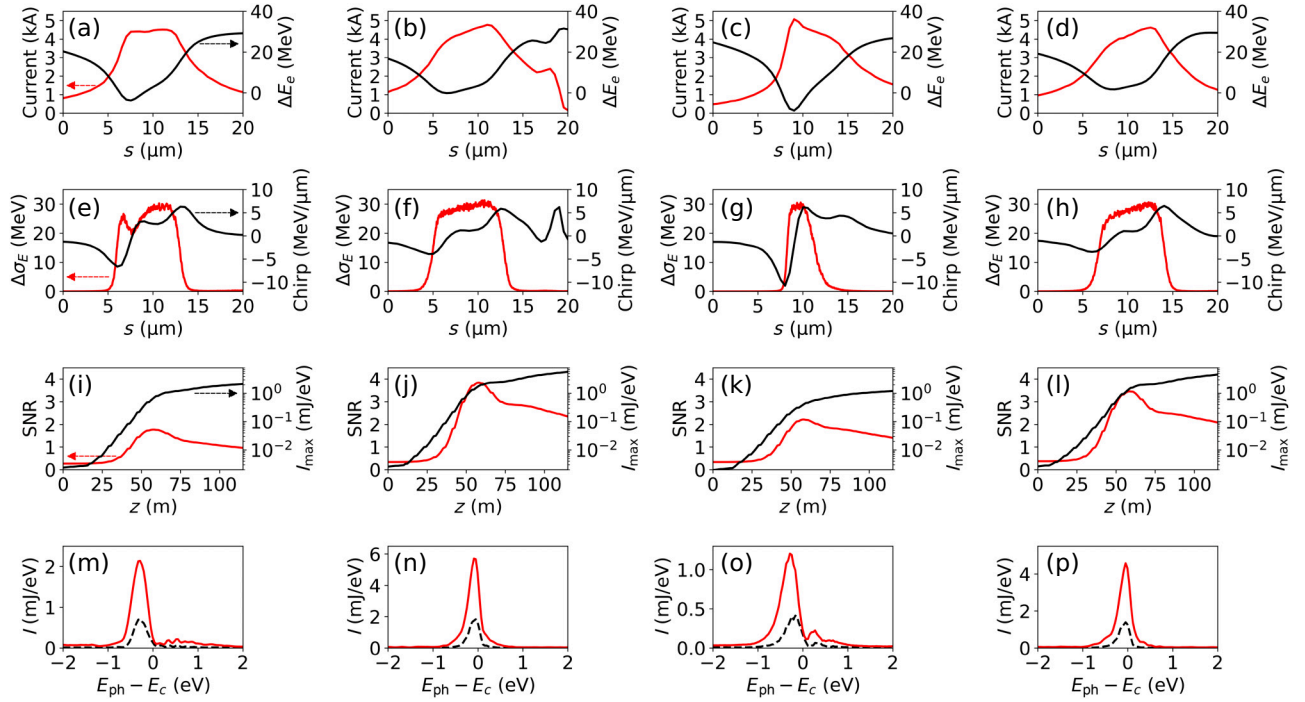


FIG. 7. Longitudinal phase space (LPS) and hard-x-ray self-seeded free-electron laser simulation results (averaged over 50 runs each) for four different cases (Case1 to Case4, corresponding to the four columns, respectively). (a)–(d) Initial LPS distributions (current profiles and relative electron beam slice center energy profiles) at the SASE2 undulator entrance. (e)–(h) Beam slice energy spread change after lasing, which indicates the lasing window, and the electron beam energy chirp calculated from the derivative of the initial energy profile from the first row. (i)–(l) Signal-to-noise ratio (SNR) and peak spectral density evolution along the undulator in the final seeding amplification stage with optimized taper setting. (m)–(p) Spectral density at the position where the SNR has a maximum value (the black dashed curves) and at the undulator exit where the peak spectral density reaches maximum values (the solid red curves), here $E_c = 9$ keV.

simultaneously influencing both the bandwidth and SNR. This correlation is particularly evident in Case3 and Case4, as shown in Fig. 7, where the energy chirp and current

TABLE II. HXRSS FEL simulation results (averaged over 50 runs for each case). Here, the C(004) reflection plane is chosen for the monochromator crystal, the impinging energy is the averaged SASE pulse energy impinging on the crystal, $z1$ is the approximated longitudinal position along the undulator in the last seeding amplification stage where the SNR has its largest value, $z2$ corresponds to the undulator exit.

Parameter	Case1	Case2	Case3	Case4	Unit
Impinging energy	38	37	26	32	μJ
Delay	10	10	12.5	10	μm
$z1$		58			m
Pulse energy	0.52	0.79	0.32	0.61	mJ
I_{max}	0.71	1.84	0.41	1.39	mJ/eV
SNR	1.77	3.84	2.22	3.46	
Bandwidth	0.32	0.24	0.40	0.28	eV
$z2$		114			m
Pulse energy	2.55	3.25	1.32	2.77	mJ
I_{max}	2.14	5.71	1.20	4.58	mJ/eV
SNR	0.97	2.36	1.42	2.09	
Bandwidth	0.36	0.28	0.44	0.28	eV

profile collectively impact the HXRSS FEL spectrum's bandwidth and SNR. Although the current profile in Fig. 7(a) is flat, the seeded lasing performance is not the best. The relatively wide bandwidth is due to the large electron beam energy chirp, while the small SNR suffers from the limited delay in order to have sufficient amplification to get a high peak spectral density. Case2 and Case4 both have their peak current at the head and they have similar HXRSS FEL performances, which are better than in the other two cases, either with the peak current at the tail or with a flat current profile.

In this section, we show from start-to-end simulations for the European XFEL SASE2 beamline that it is advantageous to have a relative flat energy profile with a peak current located at the head for HXRSS FEL applications. Cases with a peak current located at the head may give us seeding wake with a higher strength and higher purity. In addition, with the peak current at the head, there is less of a kick from the beam switchyard arc, hence the lasing window can be longer compared with cases that have the peak current at the tail. With these optimizations, the amplified HXRSS FEL spectra can have a higher spectral density with narrower bandwidth and improved SNR.

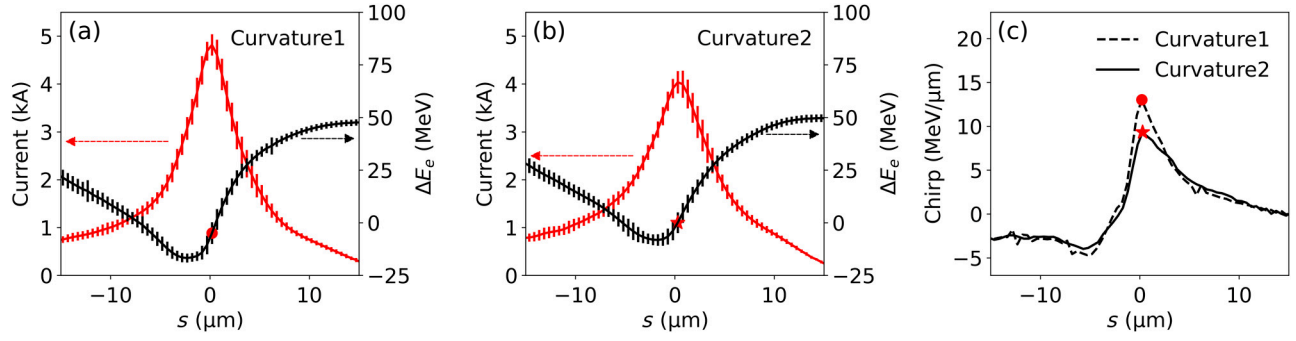


FIG. 8. Electron beam analysis from passive streaker measurements. (a),(b) Current profile and beam slice center energy for Curvature1 and Curvature2, respectively. (c) Beam energy chirp calculated from (a),(b); the maximum chirps are denoted by dot and star, respectively.

IV. EXPERIMENTAL RESULTS

A HXRSS FEL system was installed at the SASE2 beamline at the European XFEL in 2019 and the user delivery of the HXRSS FEL started in 2021. Our experiments are carried out at this setup.

Experimental results for controlling the HXRSS FEL bandwidth via manipulation of the electron beam energy chirp by tuning the curvature of the injector section are shown in Figs. 8 and 9. The LPS is measured with the passive streaker installed downstream of the SASE2 undulator [42]. HXRSS spectral bandwidth is closely related to the electron beam energy chirp within the lasing window. As

shown by Fig. 8, in the case with the unoptimized injector curvature of 180 m^{-2} (indicated by Curvature1), the non-linear chirp has a maximum value of $13.0 \text{ MeV}/\mu\text{m}$. After tuning the injector curvature by decreasing it by 26 m^{-2} down to 154 m^{-2} (indicated by Curvature2), the maximum chirp value decreases to $9.3 \text{ MeV}/\mu\text{m}$. The undulator longitudinal dispersion for the final seeding amplification part is estimated to be $R_{56,\text{undu}} = 0.48 \mu\text{m}$ and the reference electron beam energy is 16.5 GeV ; therefore, the maximum local photon energy shift is estimated to be $\Delta E_{\text{ph}} = -4.16 \text{ eV}$ for Curvature1 and -2.98 eV for Curvature2 according to Eq. (3).

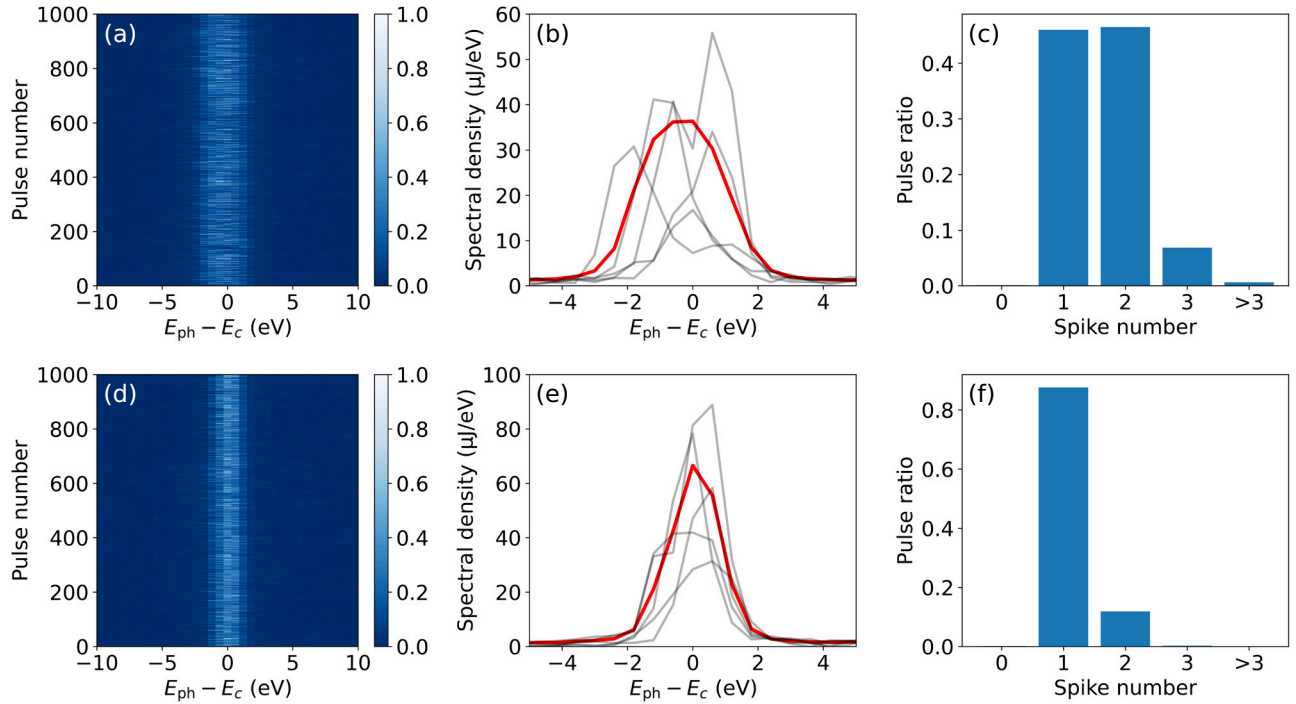


FIG. 9. Hard-x-ray self-seeded free-electron laser spectrum analysis for Curvature1 (first row) and Curvature2 (second row). The central photon energy is $E_c = 10\,872 \text{ eV}$ for both cases. (a),(d) Consecutive 1000 spectra (colored by normalized spectral intensity). (b),(e) Averaged (red curves) and single-pulse (gray curves) spectra. (c),(f) Spectral spike statistics analysis for the 1000 pulses.

Spectrum analyses for these two cases are shown in Fig. 9. We see that with the injector curvature optimized, the averaged spectral bandwidth decreases from 3.0 eV for Curvature1 down to 1.9 eV for Curvature2, and the peak spectral intensity increases accordingly (36 $\mu\text{J}/\text{eV}$ for Curvature1 with a pulse energy of 248 μJ , and 66 $\mu\text{J}/\text{eV}$ for Curvature2 with a pulse energy of 318 μJ). It should be noted here that the spectrometer resolution is rather low (0.6 eV/pixel) for this experimental study and the seeding performance is not fully optimized due to limited beam time. For reference, the typical spectrometer resolution is 0.2–0.3 eV/pixel, and the spectral density can be optimized up to 1 mJ/eV with a bandwidth of around 0.8 eV [14]. If the beam energy profile has some abrupt change with two or more dominating parts having different linear chirps within the lasing window, multiple spikes due to different photon energy shifts may appear in the spectrum, as shown by some gray curves in Fig. 9(b), so the spectrum spike number statistics, in addition to the averaged spectral bandwidth, can give us hints about the nonlinearity of the correlated energy chirp. We can see from Figs. 9(c) and 9(f) that the single spike events ratio increases from 46% in the case of Curvature1 to 88% in the case of Curvature2. Central photon energy shifts for the single pulses in Fig. 9(b) are larger than those in Fig. 9(e), qualitatively agreeing with theoretical analyses using chirp values from Fig. 8.

Examples of SNR control can be found from two consecutive user delivery weeks, where we experimentally observed seeding performance with different SNRs due to the different current profiles. The examples are shown in

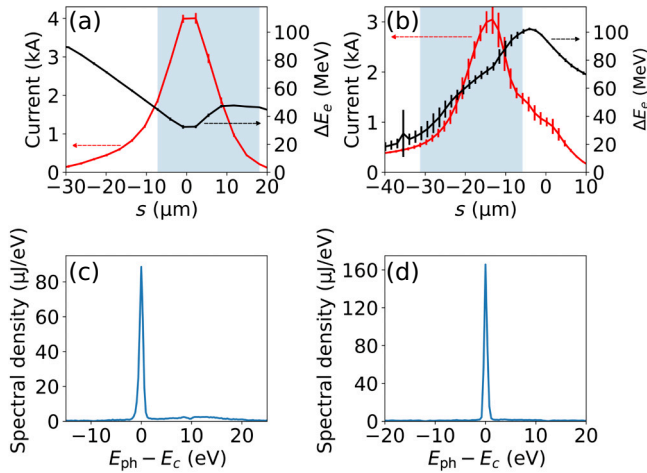


FIG. 10. (a),(b) Electron beam current profile and mean beam slice center energy reconstructed from the passive streaker measurements for two experiments. The shaded area shows the lasing window derived from the slice energy spread difference between seeded lasing on and free-electron laser (FEL) disabled. (c),(d) Averaged (over 1000 pulses) hard-x-ray self-seeded FEL spectra corresponding to (a),(b), respectively. The central photon energy is $E_c = 8573$ eV (c) and $E_c = 10605$ eV (d).

Fig. 10, where the shaded area is derived from the passive streaker measurement showing the lasing window. We see that the electron beam has the peak current at the tail within the lasing window in Fig. 10(a) and the corresponding averaged spectrum in Fig. 10(c) has a small SNR of 2.83. The electron beam with a peak current at the head within the lasing window is shown in Fig. 10(b) and the corresponding averaged spectrum in Fig. 10(d) has a larger SNR of 4.79. Meanwhile, one can also see that the SASE background in Fig. 10(c) is located on the higher photon energy side, which agrees with the start-to-end simulation in Fig. 7(o). This is due to the fact that, in the case with the peak current at the tail within the lasing window, even with a relatively large delay [delay values are optimized to maximize the peak spectral density and it is 38 fs for the case shown in Fig. 10(a) compared with 16 fs for the case shown in Fig. 10(b)], the head part with a slightly higher energy is still overlapping with the SASE generated upstream of the chicane and continues to amplify it in the final seeding amplification stage. These experimental results confirm our theoretical analysis.

V. SUMMARY AND OUTLOOK

The increasing user demands for bandwidth and SNR control in HXRSS FELs have driven the need for a comprehensive understanding of the impact of electron beam current and energy profiles on the seeding properties. In this paper, we investigate these two aspects both theoretically and experimentally. Our findings reveal a significant dependence of HXRSS spectral bandwidth on the electron beam energy profile. Specifically, we observe shifts in the central photon energy with a linear energy chirp and broadened bandwidth with a nonlinear energy chirp during the seeding amplification process. For HXRSS SNR control, we discuss a trade-off between seeding signal strength and purity, which can be easily visualized by the time-frequency analyses adopting continuous wavelet transform and short-time Fourier transform. Moreover, we demonstrate the benefits of a beam with its peak current located at the head for asymmetric current profiles both in simulations and in experiments. By optimizing the chirp, curvature, skewness, and first- and second-order derivatives of the inverse global compression, one can produce a desirable beam profile with the peak current favorably located at the head, minimizing the energy chirp within the lasing window and thereby achieving a narrower bandwidth and larger SNR.

To achieve an even narrower nearly Fourier-transform-limited spectral bandwidth, a longer lasing window for seeded FELs can be adopted, such as with a high charge operation mode, provided that a flat energy profile can be maintained. Here it should be noted that this method can work only with a relatively flat electron beam energy profile and that the bandwidth decrease due to the longer

lasing window will dominate over the bandwidth increase due to the nonlinear energy chirp. It is worth mentioning that the potential for further SNR enhancement through proper tapering remains a subject for future exploration and is outside the scope of this study. In addition, further simulation studies incorporating additional parameters, such as the transverse slice center offset derived from upgraded measurements, could help enhance the performance of the HXRSS FEL.

Together with the properly tuned beam current profile with its peak current located at the head, the increased peak spectral density and purity may further promote the unique advantage of HXRSS FELs and enable more demanding applications requiring higher resolution. The methods for HXRSS FEL bandwidth and SNR control presented in this paper can not only help with tuning for existing HXRSS FEL facilities to satisfy different user requests, but also serve as a tool box for the design and development of HXRSS FELs for future FEL facilities.

ACKNOWLEDGMENTS

We would like to acknowledge helpful discussions with Philipp Dijkstal, Naresh Kujala, Sergey Tomin, Stuart Walker, and Igor Zagorodnov. The numerical simulations were supported by the Maxwell computational resources operated at Deutsches Elektronen-Synchrotron DESY, Hamburg, Germany. T.L. acknowledges support from the 2021 Helmholtz-OCPC Fellowship Program. This work is partially supported by the National Natural Science Foundation of China (Grant No. 11975039).

DATA AVAILABILITY

The data supporting this study's findings are available within the article.

-
- [1] Z. Huang and K.-J. Kim, Review of x-ray free-electron laser theory, *Phys. Rev. Spec. Top.-Accel. Beams* **10**, 034801 (2007).
 - [2] C. Bostedt, S. Boutet, D. M. Fritz, Z. Huang, H. J. Lee, H. T. Lemke, A. Robert, W. F. Schlotter, J. J. Turner, and G. J. Williams, Linac coherent light source: The first five years, *Rev. Mod. Phys.* **88**, 015007 (2016).
 - [3] J. C. Spence, U. Weierstall, and H. Chapman, X-ray lasers for structural and dynamic biology, *Rep. Prog. Phys.* **75**, 102601 (2012).
 - [4] P. Abbamonte, F. Abild-Pedersen, P. Adams, M. Ahmed, F. Albert, R. A. Mori, P. Anfinrud, A. Aquila, M. Armstrong, and J. Arthur *et al.*, *New science opportunities enabled by LCLS-II X-ray lasers*, Tech. Rep. (institution SLAC National Accelerator Lab., Menlo Park, CA (United States), 2015).
 - [5] A. I. Chumakov, A. Q. Baron, I. Sergueev, C. Stroh, O. Leupold, Y. Shvyd'ko, G. V. Smirnov, R. Ruffer, Y. Inubushi, and M. Yabashi *et al.*, Superradiance of an ensemble of nuclei excited by a free electron laser, *Nat. Phys.* **14**, 261 (2018).
 - [6] B. Adams, G. Aeppli, T. Allison, A. Q. Baron, P. Bucksbaum, A. I. Chumakov, C. Corder, S. P. Cramer, S. DeBeer, and Y. Ding *et al.*, Scientific opportunities with an x-ray free-electron laser oscillator, [arXiv:1903.09317](https://arxiv.org/abs/1903.09317).
 - [7] C. Callegari, A. N. Grum-Grzhimailo, K. L. Ishikawa, K. C. Prince, G. Sansone, and K. Ueda, Atomic, molecular and optical physics applications of longitudinally coherent and narrow bandwidth free-electron lasers, *Physics Reports* **904**, 1 (2021).
 - [8] L. H. Yu, Generation of intense uv radiation by subharmonically seeded single-pass free-electron lasers, *Phys. Rev. A* **44**, 5178 (1991).
 - [9] G. Stupakov, Using the beam-echo effect for generation of short-wavelength radiation, *Phys. Rev. Lett.* **102**, 074801 (2009).
 - [10] G. Geloni, V. Kocharyan, and E. Saldin, A novel self-seeding scheme for hard x-ray FELs, *J. Mod. Opt.* **58**, 1391 (2011).
 - [11] J. Amann, W. Berg, V. Blank, F.-J. Decker, Y. Ding, P. Emma, Y. Feng, J. Frisch, D. Fritz, and J. Hastings *et al.*, Demonstration of self-seeding in a hard-x-ray free-electron laser, *Nat. Photonics* **6**, 693 (2012).
 - [12] I. Inoue, T. Osaka, T. Hara, T. Tanaka, T. Inagaki, T. Fukui, S. Goto, Y. Inubushi, H. Kimura, and R. Kinjo *et al.*, Generation of narrow-band x-ray free-electron laser via reflection self-seeding, *Nat. Photonics* **13**, 319 (2019).
 - [13] I. Nam, C.-K. Min, B. Oh, G. Kim, D. Na, Y. J. Suh, H. Yang, M. H. Cho, C. Kim, and M.-J. Kim *et al.*, High-brightness self-seeded x-ray free-electron laser covering the 3.5 keV to 14.6 keV range, *Nat. Photonics* **15**, 435 (2021).
 - [14] S. Liu, C. Grech, M. Guetg, S. Karabekyan, V. Kocharyan, N. Kujala, C. Lechner, T. Long, N. Mirian, and W. Qin *et al.*, Cascaded hard x-ray self-seeded free-electron laser at megahertz repetition rate, *Nat. Photonics* **17**, 984 (2023).
 - [15] Y. Shvyd'ko and R. Lindberg, Spatiotemporal response of crystals in x-ray Bragg diffraction, *Phys. Rev. Spec. Top.-Accel. Beams* **15**, 100702 (2012).
 - [16] R. R. Lindberg and Y. V. Shvyd'ko, Time dependence of Bragg forward scattering and self-seeding of hard x-ray free-electron lasers, *Phys. Rev. Spec. Top.-Accel. Beams* **15**, 050706 (2012).
 - [17] G. Geloni, V. Kocharyan, and E. Saldin, Cascade self-seeding scheme with wake monochromator for narrow-bandwidth x-ray FELs, [arXiv:1006.2045](https://arxiv.org/abs/1006.2045).
 - [18] S. Liu, W. Decking, V. Kocharyan, E. Saldin, S. Serkez, R. Shayduk, H. Sinn, and G. Geloni, Preparing for high-repetition rate hard x-ray self-seeding at the European x-ray free electron laser: Challenges and opportunities, *Phys. Rev. Accel. Beams* **22**, 060704 (2019).
 - [19] Y. Shvyd'ko, R. Röhlsberger, O. Kocharovskaya, J. Evers, G. A. Geloni, P. Liu, D. Shu, A. Miceli, B. Stone, and W. Hippler *et al.*, Resonant x-ray excitation of the nuclear clock isomer ^{45}Sc , *Nature* **622**, 471 (2023).
 - [20] R. Röhlsberger, *Nuclear Condensed Matter Physics with Synchrotron Radiation: Basic Principles, Methodology and Applications* (Springer Science & Business Media, 2004), Vol. 208.

- [21] A. I. Chumakov, A. Q. R. Baron, I. Sergueev, C. Stroh, O. Leupold, Y. Shvyd'ko, G. V. Smirnov, R. Ruffer, Y. Inubushi, M. Yabashi, K. Tono, T. Kudo, and T. Ishikawa, Superradiance of an ensemble of nuclei excited by a free electron laser, *Nat. Phys.* **14**, 261 (2018).
- [22] F. M. F. de Groot, M. W. Haverkort, H. Elnaggar, *et al.* Resonant inelastic X-ray scattering, *Nat. Rev. Methods Primers* **4**, 45 (2024).
- [23] O. Chubar, G. Geloni, V. Kocharyan, A. Madsen, E. Saldin, S. Serkez, Y. Shvyd'ko, and J. Sutter, Ultra-high-resolution inelastic x-ray scattering at high-repetition-rate self-seeded x-ray free-electron lasers, *J. Synchrotron Radiat.* **23**, 410 (2016).
- [24] X. Yang and Y. Shvyd'ko, Maximizing spectral flux from self-seeding hard x-ray free electron lasers, *Phys. Rev. Spec. Top.-Accel. Beams* **16**, 120701 (2013).
- [25] Z. Huang, A. Brachmann, F.-J. Decker, Y. Ding, D. Dowell, P. Emma, J. Frisch, S. Gilevich, G. Hays, and P. Hering *et al.*, Measurements of the linac coherent light source laser heater and its impact on the x-ray free-electron laser performance, *Phys. Rev. Spec. Top.-Accel. Beams* **13**, 020703 (2010).
- [26] Z. Zhang, R. Lindberg, W. M. Fawley, Z. Huang, J. Krzywinski, A. Lutman, G. Marcus, and A. Marinelli, Microbunching-instability-induced sidebands in a seeded free-electron laser, *Phys. Rev. Accel. Beams* **19**, 050701 (2016).
- [27] G. Marcus, W. M. Fawley, D. Bohler, Y. Ding, Y. Feng, E. Hemsing, Z. Huang, J. Krzywinski, A. Lutman, and D. Ratner, Experimental observations of seed growth and accompanying pedestal contamination in a self-seeded, soft x-ray free-electron laser, *Phys. Rev. Accel. Beams* **22**, 080702 (2019).
- [28] S. Reiche, Genesis 1.3: A fully 3D time-dependent FEL simulation code, *Nucl. Instrum. Methods Phys. Res., Sect. A: Accelerators, Spectrometers, Detectors and Associated Equipment* **429**, 243 (1999).
- [29] E. Wigner, On the quantum correction for thermodynamic equilibrium, *Phys. Rev.* **40**, 749 (1932).
- [30] M. Bastiaans, Propagation laws for the second-order moments of the Wigner distribution function in first-order optical systems, *Optik: International Journal for Light and Electron Optics* **82**, 173 (1989).
- [31] K.-J. Kim, in *AIP conference proceedings*, Vol. 184 (American Institute of Physics, 1989), p. 565.
- [32] S. Krinsky and Z. Huang, Frequency chirped self-amplified spontaneous-emission free-electron lasers, *Phys. Rev. Spec. Top.-Accel. Beams* **6**, 050702 (2003).
- [33] J. Wu, J. B. Murphy, P. J. Emma, X. Wang, T. Watanabe, and X. Zhong, Interplay of the chirps and chirped pulse compression in a high-gain seeded free-electron laser, *JOSA B* **24**, 484 (2007).
- [34] S. Serkez, Self-seeding XFELs: Operation principle and challenges, *Synchrotron Radiat. News* **29**, 10 (2016).
- [35] F. Auger, P. Flandrin, P. Gonçalves, and O. Lemoine, Time-frequency toolbox tutorial. CNRS (France), Rice U. (USA) (2005), <https://tftb.nongnu.org/tutorial.pdf>.
- [36] J. M. Lilly and S. C. Olhede, Generalized Morse wavelets as a superfamily of analytic wavelets, *IEEE Trans. Signal Process.* **60**, 6036 (2012).
- [37] J. M. Lilly and S. C. Olhede, Higher-order properties of analytic wavelets, *IEEE Trans. Signal Process.* **57**, 146 (2008).
- [38] W. Decking, S. Abeghyan, P. Abramian, A. Abramsky, A. Aguirre, C. Albrecht, P. Alou, M. Altarelli, P. Altmann, and K. Amyan *et al.*, A MHz-repetition-rate hard x-ray free-electron laser driven by a superconducting linear accelerator, *Nat. Photonics* **14**, 391 (2020).
- [39] T. Tschentscher, C. Bressler, J. Grünert, A. Madsen, A. P. Mancuso, M. Meyer, A. Scherz, H. Sinn, and U. Zastrau, Photon beam transport and scientific instruments at the European XFEL, *Appl. Sci.* **7**, 592 (2017).
- [40] U. Zastrau, K. Appel, C. Baecht, O. Baehr, L. Batchelor, A. Berghäuser, M. Banjafar, E. Brambrink, V. Cerantola, and T. E. Cowan *et al.*, The High Energy Density scientific instrument at the European XFEL, *J. Synchrotron Radiat.* **28**, 1393 (2021).
- [41] A. Madsen, J. Hallmann, G. Ansaldi, T. Roth, W. Lu, C. Kim, U. Bösenberg, A. Zozulya, J. Möller, and R. Shayduk *et al.*, Materials Imaging and Dynamics (MID) instrument at the European X-ray Free-Electron Laser facility, *J. Synchrotron Radiat.* **28**, 637 (2021).
- [42] P. Dijkstal, W. Qin, and S. Tomin, Longitudinal phase space diagnostics with a nonmovable corrugated passive wakefield streaker, *Phys. Rev. Accel. Beams* **27**, 050702 (2024).
- [43] I. Zagorodnov and M. Dohlus, Semianalytical modeling of multistage bunch compression with collective effects, *Phys. Rev. Spec. Top.-Accel. Beams* **14**, 014403 (2011).
- [44] G. Feng, I. Zagorodnov, T. Limberg, H. Jin, Y. Kot, M. Dohlus, and W. Decking, Beam dynamics simulations for European XFEL, DESY, Hamburg, Germany, Rep. TESLA-FEL **4**, 2013 (2013).
- [45] S. Liu, W. Decking, G. Feng, V. Kocharyan, I. Zagorodnov, G. Geloni, and S. Serkez, Longitudinal phase space optimization for the hard x-ray self-seeding, *Proceedings of FEL2017*, TUP004 (2017).
- [46] I. Zagorodnov, M. Dohlus, and S. Tomin, Accelerator beam dynamics at the European X-ray Free Electron Laser, *Phys. Rev. Accel. Beams* **22**, 024401 (2019).
- [47] I. Agapov, G. Geloni, S. Tomin, and I. Zagorodnov, OCELOT: A software framework for synchrotron light source and FEL studies, *Nucl. Instrum. Methods Phys. Res. Sect. A: Accelerators, Spectrometers, Detectors and Associated Equipment* **768**, 151 (2014).
- [48] W. Decking and F. Obier, Layout of the beam switchyard at the European XFEL, EPAC08-WEPC073, Genoa, Italy (2008).
- [49] V. Balandin, W. Decking, and N. Golubeva, Optics for the beam switchyard at the European XFEL, *Proc. of IPAC2011*, 2016 (2011).
- [50] T. Long, S. Huang, K. Liu, Y. Chen, W. Decking, S. Liu, N. Mirian, W. Qin, G. Geloni, and J. Yan, Phase-locked hard x-ray self-seeding FEL study for the European XFEL, FEL2022, Trieste, Italy (2022).
- [51] T. Long, Y. Chen, W. Decking, G. Geloni, N. Golubeva, S. Huang, S. Liu, W. Qin, and M. Scholz, in *Journal of Physics: Conference Series*, Vol. 2687 (IOP Publishing, 2024), p. 062021.